PHYSICAL REVIEW B **69**, 214109 (2004)

Bismuth manganite: A multiferroic with a large nonlinear optical response

Alok Sharan,[1] James Lettieri,[1,*] Yunfa Jia,[1] Wei Tian,[1] Xiaoqing Pan,[2] Darrell G. Schlom,[1] and Venkatraman Gopalan[1]
[1]*Materials Research Institute and Department of Materials Science and Engineering, Pennsylvania State University, University Park, Pennsylvania, 16802, USA*
[2]*Department of Materials Science and Engineering, The University of Michigan, Ann Arbor, Michigan, USA*

(Received 16 October 2003; revised manuscript received 19 December 2003; published 25 June 2004)

We report evidence for ferroelectricity in bismuth manganite epitaxial films from optical second-harmonic generation (SHG). The change in the polar symmetry of SHG signals under external electric fields is correlated to specific changes in the ferroelectric domain microstructures. We also observe giant enhancement of SHG by 3 to 4 orders of magnitude with effective $d_f \sim 193$ pm/V under electric fields of ~ 707 V/mm. The material also exhibits a large third-order nonlinear optical response with nonlinear absorption coefficient $\alpha_I \sim -0.08$ cm/kW and nonlinear refractive index $n_I \sim -0.53 \times 10^{-9}$ cm^2/W.

DOI: 10.1103/PhysRevB.69.214109 PACS number(s): 77.80.−e, 42.65.Ky

There is growing interest in multiferroic materials[1–3] displaying simultaneous ferromagnetism, ferroelectricity, and ferroelasticity, due to potential applications as ferroelectromagnets and in spintronics, in addition to the inherent interest in the underlying physics of the coexistence of ferroelectricity and ferromagnetism. Bismuth manganite ($BiMnO_3$), a material with the perovskite structure and predicted to be multiferroic,[3] has been previously shown to be ferromagnetic[4–7] below a transition temperature of ~105 K and a likely ferroelectric.[4] Ferroelectricity has been difficult to prove because of the lack of single crystals and the low resistance of $BiMnO_3$ films, making it difficult to associate measured dielectric hysteresis loops to ferroelectricity instead of nonlinear dielectric losses. Bismuth manganite is metastable at atmospheric pressure and has required pressures of at least 40 000 atm to synthesize in bulk form. Moreira *et al.*[4] have reported ferroelectric hysteresis loops for polycrystalline thin films and bulk powders of $BiMnO_3$, which contained some unidentified impurities phases as well. A structural phase transition from monoclinic $C2$ to an orthorhombic $Pbnm$ has been observed at a temperature of ~770 °C,[8] which is presently postulated to be a *likely* ferroelectric to paraelectric phase transition.

In this paper, we study phase pure, epitaxially grown thin films of $BiMnO_3$ on $SrTiO_3$ (111) substrates. We correlate observed permanent changes in the magnitude and symmetry of optical second harmonic generation signals to changes in the ferroelectric domain microstructure upon applying external electric fields to the film. The large nonlinear optical responses observed in this manuscript open up possibilities for device applications exploiting all three features of ferroelectricity, ferromagnetism, and optical nonlinearity.

The magnetic point group of $BiMnO_3$ has been reported to be 2, with lattice parameters of $a = 9.5323$ Å, $b = 5.6064$ Å, and $c = 9.8535$ Å, $\alpha = \gamma = 90°$, and $\beta = 110.667°$, at room temperature (Fig. 1).[9] Symmetry dictates that the ferroelectric polarization P_s if it exists, should be along the twofold rotation axis, since this axis will destroy any polarization vector component $\mathbf{P}_{s\perp}$ perpendicular to it, by requiring an equal and opposite vector $-\mathbf{P}_{s\perp}$. Recent neutron diffraction studies indicate that the magnetic polarization is also oriented along the twofold axis. Magnetic measurements of an epitaxial $BiMnO_3$ film grown in the same way as the films in this study on a (100) $SrTiO_3$ substrate reveal a ferromagnetic transition at $T_c = 97$ K, slightly lower than the $T_c = 105$ K value of bulk $BiMnO_3$ samples.[9]

Epitaxial $BiMnO_3$ thin films were synthesized by pulsed laser deposition on (111) $SrTiO_3$ substrates using a bismuth-rich target with composition $Bi_{2.4}MnO_x$. The parameters used to grow the samples studied were a substrate temperature of 755–758 °C, an oxygen pressure of 150 mTorr, a laser fluence of 1.5–2 J/cm^2, and a laser repetition rate of 4 Hz using a 248 nm excimer laser. The samples were quenched at the completion of growth in 1 atm of oxygen to minimize bismuth desorption from the film during the cooling process. Additional details on the film deposition, structural and magnetic characterization are reported elsewhere.[10] Just as detailed structural characterization of epitaxial $BiMiO_3$ films, grown on (100) $SrTiO_3$ is consistent with the films being monoclinic.[10] our structural characterization of these epitaxial $BiMnO_3$ films grown on (111)

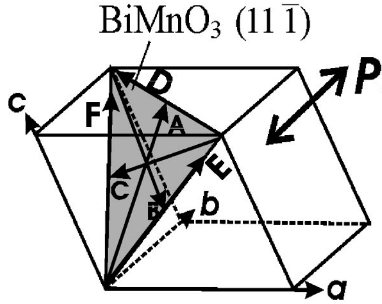

FIG. 1. A unit cell of $BiMnO_3$ indicating the polarization direction (P_s) and the growth plane for the films studied. The vector $\hat{x}_\perp$ is defined as, $\hat{x}_\perp = \hat{b} \times \hat{c}$. Various angles are defined, for example, as $\theta_{-\hat{C}\hat{x}_\perp} = \cos^{-1} l_{-\hat{C}\hat{x}_\perp}$, where $\theta_{-\hat{C}\hat{x}_\perp}$ is the angle between unit vectors $-\hat{C}$ and $\hat{x}_\perp$. These angles are $\theta_{\hat{A}\hat{a}} = 82.380°$, $\theta_{\hat{A}\hat{b}} = 73.240°$, $\theta_{\hat{A}\hat{c}} = 32.798°$, $\theta_{\hat{A}\hat{x}_\perp} = 62.695°$, $\theta_{\hat{B}\hat{a}} = 48.132°$, $\theta_{-\hat{B}\hat{b}} = 54.885°$, $\theta_{-\hat{B}\hat{c}} = 47.307°$, $\theta_{\hat{B}\hat{x}_\perp} = 62.770°$, $\theta_{\hat{C}\hat{a}} = 34.694°$, $\theta_{\hat{C}\hat{b}} = 72.798°$, $\theta_{-\hat{C}\hat{c}_\perp} = 80.512°$, $\theta_{-\hat{C}\hat{x}_\perp} = 19.790°$, $\theta_{\hat{D}\hat{a}} = 30.460°$, $\theta_{\hat{D}\hat{b}} = 59.538°$, $\theta_{\hat{D}\hat{c}} = 72.288°$, $\theta_{-\hat{D}\hat{x}_\perp} = 36.245°$, $\theta_{\hat{E}\hat{a}} = 56.706°$; $\theta_{\hat{E}\hat{b}} = 0°$, $\theta_{\hat{E}\hat{c}} = 53.96°$, $\theta_{\hat{E}\hat{x}_\perp} = 36.039°$, $\theta_{\hat{F}\hat{a}} = 72.13°$, $\theta_{\hat{F}\hat{b}} = 60.36°$, $\theta_{\hat{F}\hat{c}} = 29.638°$, and $\theta_{\hat{F}\hat{x}_\perp} = 90°$.

0163-1829/2004/69(21)/214109(7)/$22.50

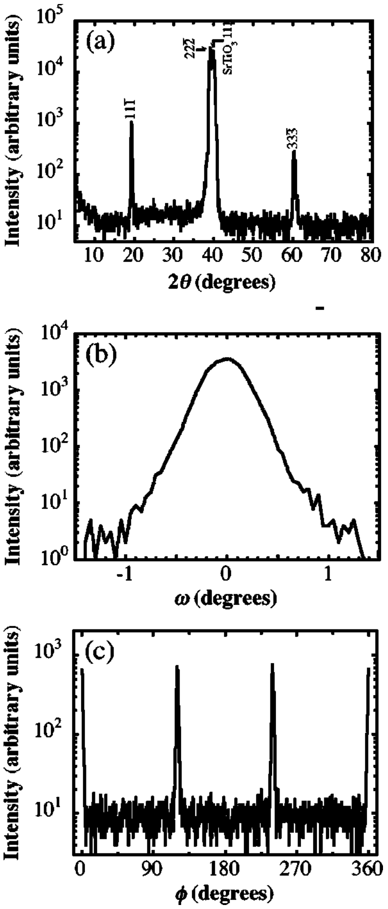

FIG. 2. (a) (θ–2θ) x-ray diffraction scan of one of the $BiMnO_3$ films used in this study grown on a $SrTiO_3$ (111) substrate. The scan reveals a nearly phase-pure ($11\bar{1}$) oriented $BiMnO_3$ film. The full width at half maximum (FWHM) of $22\bar{2}$ reflection of $BiMnO_3$ is 0.24° in 2θ. (b) Rocking curve of the $22\bar{2}$ peak of this same $BiMnO_3$ film with a FWHM of 0.39° in ω. (c) φ-scan of the 110 peak at $\chi = 61.5°$ of the ($11\bar{1}$) oriented $BiMnO_3$ film with a FWHM in φ of $\sim$1.7°. ($\chi = 90°$ aligns the diffraction vector to be perpendicular to the plane of the substrate). $\varphi = 0°$ is aligned to be parallel to the $SrTiO_3$ [$\bar{1}2\bar{1}$] in-plane orientation.

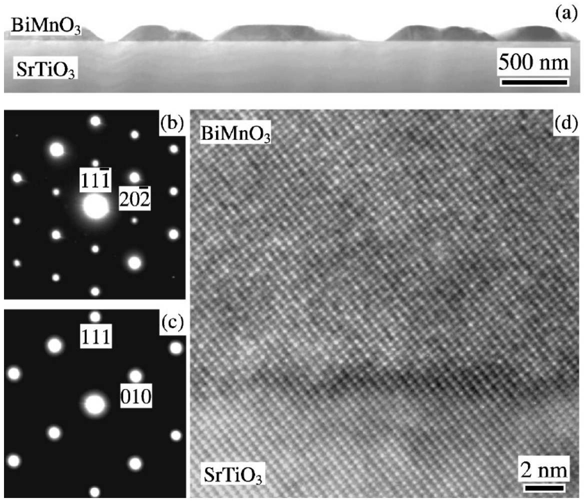

FIG. 3. (a) Low-magnification TEM image showing a cross-sectional view of one of the $BiMnO_3$ films used in this study grown on a (111) $SrTiO_3$ substrate. (b) and (c) The [101] zone axis SAED pattern of $BiMnO_3$ and the [$10\bar{1}$] zone axis SAED pattern of $SrTiO_3$ taken with the incident electron beam along the same direction, respectively. Electron diffraction studies of the film and the substrate confirm the epitaxial orientation established by x-ray studies. (d) HRTEM image of the $BiMnO_3/SrTiO_3$ interface imaged by the electron beam along the [$10\bar{1}$] zone axis of $SrTiO_3$. The HRTEM image reveals a clean interface.

$SrTiO_3$ is also consistent with the films being monoclinic. Monoclinic indices are thus used throughout this manuscript to describe the crystallography of these $BiMnO_3$ films. The films studied here are phase-pure films with the following epitaxial orientation relationship: $BiMnO_3$ ($11\bar{1}$)//$SrTiO_3$ (111), with in-plane orientations of [$\bar{1}10$] $BiMnO_3$//[$10\bar{1}$]$SrTiO_3$ (exact relation) and [112] $BiMnO_3$//[$\bar{1}2\bar{1}$] $SrTiO_3$ (approximate relation). Figure 2(a) shows a (θ-2θ) x-ray diffraction scan of one of the $BiMnO_3$ films studied. The scan reveals a phase-pure $BiMnO_3$ film with its ($11\bar{1}$) plane parallel to the (111) plane of the $SrTiO_3$ substrate. The full width at half maximum (FWHM) of the $22\bar{2}$ reflection of $BiMnO_3$ is 0.24° and 0.39° in 2θ and ω [Fig. 2(b)], respectively. Figure 2(c) shows a φ scan of the 110 peak of the ($11\bar{1}$)-oriented $BiMnO_3$ film with a FWHM in φ of $\sim$1.7°. The interplanar spacing between the $BiMnO_3$ ($11\bar{1}$) planes, $d_{(11\bar{1})}$, deduced from the peak positions in Fig. 2(a) and the standard correction for the sample height error is $d_{(11\bar{1})} = 4.604 \pm 0.001$ Å. This close to the $d_{(11\bar{1})} = 4.585$ Å spacing of bulk $BiMnO_3$.

The microstructure of one of the same films whose optical properties were investigated was studied by cross-sectional transmission electron microscopy (TEM). The results are shown in Fig. 3. Figure 3(a) shows a low-magnification cross-sectional TEM image of the film. The TEM images revealed no evidence of impurity or amorphous phases. Figures 3(b) and 3(c) are selected-area electron diffraction (SAED) patterns taken from the film and the substrate, respectively, with the incident electron beam along the same direction. They are, respectively, identified to be the [101] zone axis SAED pattern of monoclinic $BiMnO_3$ and the [$10\bar{1}$] zone axis SAED pattern of $SrTiO_3$. The electron diffraction patterns observed were consistent with the film having the same monoclinic structure as bulk $BiMnO_3$ samples and the orientation relationship determined from TEM corroborated that deduced from the four-circle x-ray diffraction measurements. Figure 3(d) shows a high-resolution TEM (HRTEM) image of the film/substrate interface. The HRTEM image reveals that the interface is clean.

Figure 4 shows the 12 types of ferroelectric domain variants that can exist in these films. Both ferroelectricity and electric-dipole second harmonic generation (SHG) occur only in noncentrosymmetric media. Since the monoclinic space group ($C2$) of $BiMnO_3$ is noncentrosymmetric, one would expect SHG signals. However, to establish ferroelectricity one has to see the changes in the ferroelectric polarization direction with applied external fields. The consequent

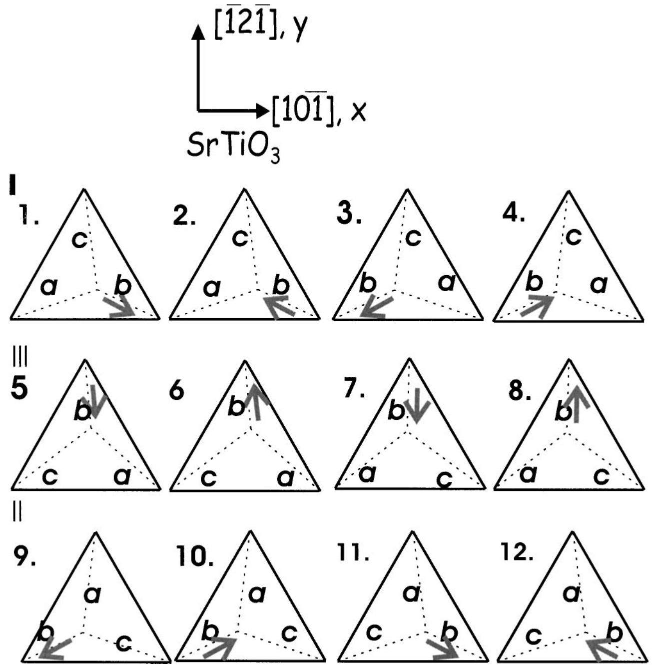

FIG. 4. Plan view of the growth plane with 12 different possible domain variants in an epitaxial thin film of BiMnO$_3$. The broken lines are the projection of the *a*, *b*, and *c* unit-cell axes on the growth plane. Arrows indicate the projection of P_s on the growth plane. At room temperature, the ferroelectric polarization (*b* axis) is tilted at an angle of ~54.88°, and *a* and *c* axes at ~34.69° and ~32.80°, respectively, from the growth plane.

changes in the magnitude, and in particular, *symmetry* of second harmonic response with applied external fields can provide unique signatures of the presence and rearrangement of ferroelectric domains.[11–13]

SHG experiments were performed using a tunable Ti-sapphire laser with 65 fs pulses of $\lambda = 900$ nm fundamental light. The laser pulses were incident from the substrate side at a repetition rate of 82 MHz with an average power of ~400 mW over a probed beam with a 126 μm diameter beam incident on the film. The SHG signal was detected using a line filter around 450 nm, and using a lock-in technique. Under identical conditions, *no* SHG signals were observed from a bare SrTiO$_3$(111) substrate with or without applied fields. Electric fields were applied *in situ* while SHG measurements were performed. Since the film exhibited large dielectric losses at room temperature and above, Au electrode pads were applied to the backside of the SrTiO$_3$ substrate, with a spacing of 2 mm, and voltages of up to ±2 kV were applied as shown in the inset of Fig. 7. Using a relative dielectric constant of 448 for the 0.87-mm-thick SrTiO$_3$ substrate at room temperature, and not accounting for the presence of the film, the actual fields at the interface between the film and the substrate were estimated to be of the order of 707 V/mm parallel to the interface. We have not attempted to apply Au pads on the film side for measurement at lower temperatures (82 K) where dielectric losses may be lower.

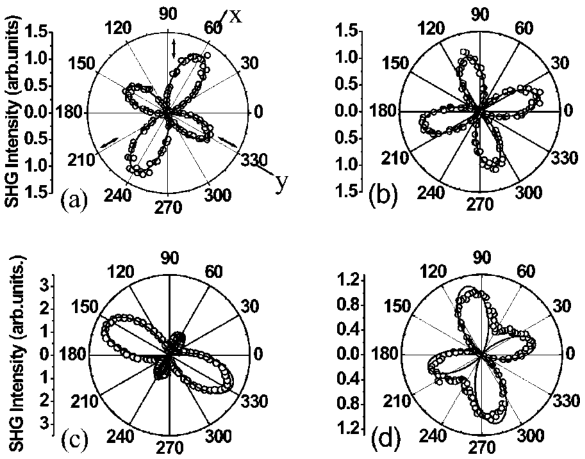

FIG. 5. Polar plots at 82 K of the SHG intensity polarized along either the SrTiO$_3$ $[10\bar{1}]$ [denoted as the *x* axis; intensity I_x (b) and (d)] or $[\bar{1}2\bar{1}]$ [denoted as the *y* axis, intensity I_y (a) and (c)] as a function of the input polarization direction of the fundamental beam at an angle θ to the *x* axis. Plots (a) and (b) correspond to before application of any voltage, and plots (c) and (d) correspond to after application and removal of a voltage of -2 kV. Circles are experimental points and solid lines are theoretical fits based on Eq. (3). Double-headed arrows in (a) indicate the projection of possible ferroelectric polarization directions P_s shown in Fig. 1 on to the film growth plane, also the plane of the plots.

Figure 5 shows the polar plots at a temperature of 82 K, of the SHG intensity ($\lambda = 450$ nm) polarized along either the SrTiO$_3$ $[10\bar{1}]$ direction (denoted as the *x* axis; intensity I_x in [Figs. 5(b), 5(d)]) or the SrTiO$_3$ $[\bar{1}2\bar{1}]$ direction (denoted as the *y* axis, intensity I_y in [Figs. 5(a), 5(c)]) as a function of the input polarization direction of the fundamental beam ($\lambda = 900$ nm) at an angle θ to the *x* axis. The local nonlinear polarization $P_i^{2\omega}$ (*i* denotes *local* unit-cell coordinates) are calculated for each domain variant in Fig. 4, and summed, taking their relative phases into account. The *total* nonlinear polarization $P_j^{2\omega}$ ($j = x$ or *y*, which are *global* coordinates), in the film created by the fundamental beam can thus be derived as

$$\begin{aligned} P_j^{2\omega} = {} & (A_{\mathrm{I},j} + A_{\mathrm{II},j} e^{i\Gamma_{\mathrm{II},j}} + A_{\mathrm{III},j} e^{i\Gamma_{\mathrm{III},j}}) \cos^2\theta \\ & + (B_{\mathrm{I},j} + B_{\mathrm{II},j} e^{i\Gamma_{\mathrm{II},j}} + B_{\mathrm{III},j} e^{i\Gamma_{\mathrm{III},j}}) \sin^2\theta \\ & + (C_{\mathrm{I},j} + C_{\mathrm{II},j} e^{i\Gamma_{\mathrm{II},j}} + C_{\mathrm{III},j} e^{i\Gamma_{\mathrm{III},j}}) \sin(2\theta), \end{aligned} \tag{1}$$

where, referring to Fig. 4, the terms $A_{K,j}$, $B_{K,j}$, and $C_{K,j}$ are the *net* contributions from the domains set $K(=\mathrm{I,II,III})$. They are listed in Table I. The terms $\Gamma_{\mathrm{II},j}$ and $\Gamma_{\mathrm{III},j}$ are relative phase shifts of the SHG contribution from domain sets II and III *with respect to* set I. The second harmonic intensity I_j is obtained as

$$\begin{aligned} I_j \propto \sum_{m,n} & (A_{m,j}\cos^2\theta + B_{m,j}\sin^2\theta + C_{m,j}\sin 2\theta)(A_{n,j}\cos^2\theta \\ & + B_{n,j}\sin^2\theta + C_{n,j}\sin 2\theta)\cos(\Gamma_{m,j} - \Gamma_{n,j}), \end{aligned} \tag{2}$$

where *m*, $n = \mathrm{I}$, II, III refer to the three domain sets I, II, and III, respectively, and we are free to choose the arbitrary phase $\Gamma_{\mathrm{I},j} = 0$ according to Eq. (1). If we assume, for simplification, that all $\Gamma_{m,j} = 0$, then Eq. (2) simplifies to

TABLE I. The parameters in Eq. (3) as a function of domain fractions $f_k(k=1-12)$ shown in Fig. 4. The functions F and G are listed below in Tables II and III, respectively. Subscripts and superscripts accompanying F and G refer to the specific parameters they are associated with in column 1.

Parameters	$j=x$, SrTiO$_3$ $[10\overline{1}]$	$j=y$, SrTiO$_3$ $[\overline{1}2\overline{1}]$
$A_{\mathrm{I},j}$	$f_{1+4-2-3}F^A_{\mathrm{I},x}+f_{1+2-3-4}G^A_{\mathrm{I},x}$	$f_{1+3-2-4}F^A_{\mathrm{I},y}+f_{1+2+3+4}G^A_{\mathrm{I},y}$
$A_{\mathrm{II},j}$	$f_{5+6-7-8}G^A_{\mathrm{II},x}$	$f_{5+7-6-8}F^A_{\mathrm{II},y}+f_{5+6+7+8}G^A_{\mathrm{II},y}$
$A_{\mathrm{III},j}$	$f_{10+11-9-12}F^A_{\mathrm{III},x}$	$f_{9+11-10-12}F^A_{\mathrm{III},y}$
$B_{\mathrm{I},x}$	$f_{1+4-2-3}F^B_{\mathrm{I},x}+f_{1+2-3-4}G^B_{\mathrm{I},x}$	$f_{1+3-2-4}F^B_{\mathrm{I},y}+f_{1+2+3+4}G^B_{\mathrm{I},y}$
$B_{\mathrm{II},j}$	$f_{5+8-6-7}F^B_{\mathrm{II},x}+f_{5+6-7-8}G^B_{\mathrm{II},x}$	$f_{5+7-6-8}F^B_{\mathrm{II},y}+f_{5+6+7+8}G^B_{\mathrm{II},y}$
$B_{\mathrm{III},j}$	$f_{10+11-9-12}F^B_{\mathrm{III},x}+f_{11+12-9-10}G^B_{\mathrm{III},x}$	$f_{9+11-10-12}F^B_{\mathrm{III},y}+f_{9+10+11+12}G^B_{\mathrm{III},y}$
$C_{\mathrm{I},j}$	$f_{1+3-2-4}F^C_{\mathrm{I},x}+f_{1+2+3+4}G^C_{\mathrm{I},x}$	$f_{1+4-2-3}F^C_{\mathrm{I},y}+f_{1+2-3-4}G^C_{\mathrm{I},y}$
$C_{\mathrm{II},j}$	$f_{5+7-6-8}F^C_{\mathrm{II},x}+f_{5+6+7+8}G^C_{\mathrm{II},x}$	$f_{5+8-6-7}F^C_{\mathrm{II},y}+f_{5+6-7-8}G^C_{\mathrm{II},y}$
$C_{\mathrm{III},j}$	$f_{9+11-10-12}F^C_{\mathrm{III},x}+f_{9+10+11+12}G^C_{\mathrm{III},x}$	$f_{10+11-9-12}F^C_{\mathrm{III},y}+f_{11+12-9-10}G^C_{\mathrm{III},y}$

$$I_j\propto(A_j\cos^2\theta+B_j\sin^2\theta+C_j\sin 2\theta)^2, \qquad (3)$$

where $A_j=\Sigma_m A_{m,j}$ and similarly for B_j and C_j. Theoretical fits based on Eq. (3) are shown in Fig. 5 as solid lines. As shown in Figs. 5(c) and 5(d), one also observes that, at 82 K, these polar plots show permanent changes when an external step voltage of $+2$ kV is applied along the $+y$ direction for a period of 30 min and then shut off. These permanent changes are discussed below.

We emphasize the qualitative physical implications of fitting parameters in Eq. (3) and Table I from a domain microstructure perspective. Within a two-dimensional microstructure assumption for the thin film, and within the probe area of the beam, let us define f_k as the area fraction of any one of $k=1-12$ domain variants in Fig. 4. Abbreviated notation such as $f_{1+3-2-4}=f_1+f_3-f_2-f_4$ is adopted. The constants F in Table I are linear functions of nonlinear coefficients d_{34}, d_{21}, d_{22}, d_{23}, d_{16} and cosines of various geo-

TABLE II. Explicit dependence of function F (in Table I) on nonlinear coefficients d_{34}, d_{21}, d_{22}, d_{23} d_{16} and cosines of various geometric angles. Subscripts $K=$I, II, III refer to three domain sets as shown in Fig. 4.

K	j	$F_{K,j}$
$K=$I	$j=x$	$F^A_{\mathrm{I},x}=l_{\hat{D}\hat{b}}[d_{34}l^2_{\hat{D}\hat{c}}+(d_{21}+d_{16})l^2_{-\hat{D}\hat{x}_\perp}+d_{22}l^2_{\hat{D}\hat{b}}+d_{23}l^2_{\hat{D}\hat{c}}]$
		$F^B_{\mathrm{I},x}=d_{34}l_{\hat{D}\hat{c}}l_{\hat{A}\hat{c}}l_{\hat{A}\hat{b}}+l_{\hat{D}\hat{b}}(d_{21}l^2_{\hat{A}\hat{x}_\perp}+d_{22}l^2_{\hat{A}\hat{b}}+d_{23}l^2_{\hat{A}\hat{c}})-d_{16}l_{-\hat{D}\hat{x}_\perp}l_{\hat{A}\hat{b}}l_{\hat{A}\hat{x}_\perp}$
		$F^C_{\mathrm{I},x}=1/2\{-d_{34}(l^2_{\hat{D}\hat{c}}l_{\hat{A}\hat{b}}+l_{\hat{A}\hat{c}}l_{\hat{D}\hat{b}}l_{\hat{D}\hat{c}})+l_{\hat{D}\hat{b}}(2d_{21}l_{\hat{A}\hat{x}_\perp}l_{-\hat{D}\hat{x}_\perp}-2d_{22}l_{\hat{D}\hat{b}}l_{\hat{A}\hat{b}}-2d_{23}l_{\hat{D}\hat{c}}l_{\hat{A}\hat{c}})$ $+d_{16}l_{-\hat{D}\hat{x}_\perp}(l_{\hat{D}\hat{b}}l_{\hat{A}\hat{x}_\perp}-l_{\hat{A}\hat{b}}l_{-\hat{D}\hat{x}_\perp})\}$
	$j=y$	$F^A_{\mathrm{I},y}=-d_{34}l_{\hat{D}\hat{c}}l_{\hat{D}\hat{b}}l_{\hat{A}\hat{c}}-l_{\hat{A}\hat{b}}(d_{21}l^2_{-\hat{D}\hat{x}_\perp}+d_{22}l^2_{\hat{D}\hat{b}}+d_{23}l^2_{\hat{D}\hat{c}})+d_{16}l_{\hat{D}\hat{b}}l_{-\hat{D}\hat{x}_\perp}l_{\hat{A}\hat{x}_\perp}$
		$F^B_{\mathrm{I},y}=-d_{34}l^2_{\hat{A}\hat{c}}l_{\hat{A}\hat{b}}-l_{\hat{A}\hat{b}}(d_{21}l^2_{\hat{A}\hat{x}_\perp}+d_{22}l^2_{\hat{A}\hat{b}}+d_{23}l^2_{\hat{A}\hat{c}})-d_{16}l^2_{\hat{A}\hat{x}_\perp}l_{\hat{A}\hat{b}}$
		$F^C_{\mathrm{I},y}=1/2\{d_{34}(l_{\hat{A}\hat{c}}l_{\hat{A}\hat{b}}l_{\hat{D}\hat{c}}+l^2_{\hat{A}\hat{c}}l_{\hat{D}\hat{b}})-l_{\hat{A}\hat{b}}(2d_{12}l_{-\hat{D}\hat{x}_\perp}l_{\hat{A}\hat{x}_\perp}-2d_{22}l_{\hat{D}\hat{b}}l_{\hat{A}\hat{b}}-2d_{23}l_{\hat{D}\hat{c}}l_{\hat{A}\hat{c}})$ $+d_{16}l_{\hat{A}\hat{x}_\perp}(l_{\hat{D}\hat{b}}l_{\hat{A}\hat{x}_\perp}-l_{\hat{A}\hat{b}}l_{-\hat{D}\hat{x}_\perp})\}$
$K=$II	$j=x$	$F^A_{\mathrm{II},x}=0$
		$F^B_{\mathrm{II},x}=-d_{34}l_{\hat{E}\hat{c}}l_{-\hat{B}\hat{c}}l_{-\hat{B}\hat{b}}+d_{16}l_{\hat{E}\hat{x}_\perp}l_{-\hat{B}\hat{b}}l_{\hat{B}\hat{x}_\perp}$
		$F^C_{\mathrm{II},x}=-1/2\{d_{34}l^2_{\hat{E}\hat{c}}l_{-\hat{B}\hat{b}}+d_{16}l_{-\hat{B}\hat{b}}l^2_{\hat{E}\hat{x}_\perp}\}$
	$j=y$	$F^A_{\mathrm{II},y}=-l_{-\hat{B}\hat{b}}(d_{21}l^2_{\hat{E}\hat{x}_\perp}+d_{23}l^2_{\hat{E}\hat{c}})$
		$F^B_{\mathrm{II},y}=-\{d_{34}l^2_{-\hat{B}\hat{c}}l_{-\hat{B}\hat{b}}+l_{-\hat{B}\hat{b}}(d_{21}l^2_{\hat{B}\hat{x}_\perp}+d_{22}l^2_{-\hat{B}\hat{b}}+d_{23}l^2_{-\hat{B}\hat{c}})+d_{16}l^2_{\hat{B}\hat{x}_\perp}l_{-\hat{B}\hat{b}}\}$
		$F^C_{\mathrm{II},y}=-1/2\{l_{-\hat{B}\hat{b}}(d_{34}l_{-\hat{B}\hat{c}}l_{\hat{E}\hat{c}}-2d_{21}l_{\hat{E}\hat{x}_\perp}l_{\hat{B}\hat{x}_\perp}+2d_{23}l_{\hat{E}\hat{c}}l_{-\hat{B}\hat{c}}-d_{16}l_{\hat{B}\hat{x}_\perp}l_{\hat{E}\hat{x}_\perp})\}$
$K=$III	$j=x$	$F^A_{\mathrm{III},x}=l_{\hat{F}\hat{b}}(d_{22}l^2_{\hat{F}\hat{b}}+d_{23}l^2_{\hat{F}\hat{c}})+d_{34}l^2_{\hat{F}\hat{c}}l_{\hat{F}\hat{b}}$
		$F^B_{\mathrm{III},x}=-[d_{34}l_{\hat{F}\hat{c}}l_{-\hat{C}\hat{c}}l_{\hat{C}\hat{b}}-l_{\hat{F}\hat{b}}(d_{22}l^2_{\hat{C}\hat{b}}+d_{21}l^2_{-\hat{C}\hat{x}_\perp}+d_{23}l^2_{-\hat{C}\hat{c}})]$
		$F^C_{\mathrm{III},x}=1/2\{l_{\hat{F}\hat{b}}(-2d_{22}l_{\hat{F}\hat{b}}l_{\hat{C}\hat{b}}+2d_{23}l_{\hat{F}\hat{c}}l_{-\hat{C}\hat{c}})$ $+d_{34}l_{\hat{F}\hat{c}}(-l_{\hat{F}\hat{b}}l_{-\hat{C}\hat{c}}+l_{\hat{C}\hat{b}}l_{\hat{F}\hat{c}})\}$
	$j=y$	$F^A_{\mathrm{III},y}=-l_{\hat{C}\hat{b}}(d_{22}l^2_{\hat{F}\hat{b}}+d_{23}l^2_{\hat{F}\hat{c}})+d_{34}l_{-\hat{C}\hat{c}}l_{\hat{F}\hat{c}}l_{\hat{F}\hat{b}}$
		$F^B_{\mathrm{III},y}=-d_{16}l^2_{-\hat{C}\hat{x}_\perp}l_{\hat{C}\hat{b}}-l_{\hat{C}\hat{b}}[d_{22}l^2_{\hat{C}\hat{b}}+(d_{23}+d_{34})l^2_{-\hat{C}\hat{c}}+d_{21}l^2_{-\hat{C}\hat{x}_\perp}]$
		$F^C_{\mathrm{III},y}=1/2\{d_{16}l^2_{-\hat{C}\hat{x}_\perp}l_{\hat{F}\hat{b}}-l_{\hat{C}\hat{b}}(-2d_{22}l_{\hat{F}\hat{b}}l_{\hat{C}\hat{b}}+2d_{23}l_{\hat{F}\hat{c}}l_{-\hat{C}\hat{c}})$ $-d_{34}l_{-\hat{C}\hat{c}}(-l_{\hat{F}\hat{b}}l_{-\hat{C}\hat{c}}+l_{\hat{C}\hat{b}}l_{\hat{F}\hat{c}})\}$

TABLE III. Explicit dependence of function G (in Table I) on nonlinear coefficients d_{36}, d_{25}, d_{14}, and cosines of various geometric angles. Subscripts $K=$I, II, III refer to three domain sets as shown in Fig. 4.

K	j	$G_{K,j}$
$K=$I	$j=x$	$G^{A}_{\mathrm{I},x}=l_{\hat{D}\hat{c}}l_{-\hat{D}\hat{x}_{\perp}}[-(d_{36}+d_{25})l_{\hat{D}\hat{b}}-d_{14}l_{-\hat{D}\hat{x}_{\perp}}]$
		$G^{B}_{\mathrm{I},x}=l_{\hat{A}\hat{x}_{\perp}}[d_{36}l_{\hat{A}\hat{b}}l_{\hat{D}\hat{c}}+l_{\hat{A}\hat{c}}(d_{25}l_{\hat{D}\hat{b}}+d_{14}l_{-\hat{D}\hat{x}_{\perp}})]$
		$G^{C}_{\mathrm{I},x}=1/2\{[-d_{36}l_{\hat{D}\hat{c}}(l_{\hat{D}\hat{b}}l_{\hat{A}\hat{x}_{\perp}}-l_{\hat{A}\hat{b}}l_{-\hat{D}\hat{x}_{\perp}})]+d_{25}l_{\hat{D}\hat{b}}(l_{-\hat{D}\hat{x}_{\perp}}l_{\hat{A}\hat{c}}-l_{\hat{A}\hat{x}_{\perp}}l_{\hat{D}\hat{c}})$ $+d_{14}l_{-\hat{D}\hat{x}_{\perp}}(l_{-\hat{D}\hat{x}_{\perp}}l_{\hat{A}\hat{c}}-l_{\hat{A}\hat{x}_{\perp}}l_{\hat{D}\hat{c}})\}$
	$j=y$	$G^{A}_{\mathrm{I},y}=l_{-\hat{D}\hat{x}_{\perp}}[d_{36}l_{\hat{D}\hat{b}}l_{\hat{A}\hat{c}}+l_{\hat{D}\hat{c}}(d_{25}l_{\hat{A}\hat{b}}-d_{14}l_{\hat{A}\hat{x}_{\perp}})]$
		$G^{B}_{\mathrm{I},y}=l_{\hat{A}\hat{c}}l_{\hat{A}\hat{x}_{\perp}}[-(d_{36}+d_{25})l_{\hat{A}\hat{b}}+d_{14}l_{\hat{A}\hat{x}_{\perp}}]$
		$G^{C}_{\mathrm{I},y}=1/2\{[d_{36}l_{\hat{A}\hat{c}}(l_{\hat{D}\hat{b}}l_{\hat{A}\hat{x}_{\perp}}-l_{\hat{A}\hat{b}}l_{-\hat{D}\hat{x}_{\perp}})]-d_{25}l_{\hat{A}\hat{b}}(l_{-\hat{D}\hat{x}_{\perp}}l_{\hat{A}\hat{c}}-l_{\hat{A}\hat{x}_{\perp}}l_{\hat{D}\hat{c}})$ $+d_{14}l_{\hat{A}\hat{x}_{\perp}}(l_{-\hat{D}\hat{x}_{\perp}}l_{\hat{A}\hat{c}}-l_{\hat{A}\hat{x}_{\perp}}l_{\hat{D}\hat{c}})\}$
$K=$II	$j=x$	$G^{A}_{\mathrm{II},x}=-d_{14}l^{2}_{\hat{E}\hat{x}_{\perp}}l_{\hat{B}\hat{c}}$
		$G^{B}_{\mathrm{II},x}=l_{\hat{B}\hat{x}_{\perp}}(-d_{36}l_{-\hat{B}\hat{b}}l_{\hat{E}\hat{c}}+d_{14}l_{\hat{E}\hat{x}_{\perp}}l_{-\hat{B}\hat{c}})$
		$G^{C}_{\mathrm{II},x}=1/2\{l_{\hat{E}\hat{x}_{\perp}}[d_{36}l_{\hat{E}\hat{c}}l_{-\hat{B}\hat{b}}-d_{14}(l_{\hat{E}\hat{x}_{\perp}}l_{-\hat{B}\hat{c}}-l_{\hat{B}\hat{x}_{\perp}}l_{\hat{E}\hat{c}})]\}$
	$j=y$	$G^{A}_{\mathrm{II},y}=l_{\hat{E}\hat{x}_{\perp}}(d_{25}l_{-\hat{B}\hat{b}}l_{\hat{E}\hat{c}}+d_{14}l_{\hat{B}\hat{x}_{\perp}}l_{\hat{E}\hat{c}})$
		$G^{B}_{\mathrm{II},y}=-l_{-\hat{B}\hat{c}}(d_{36}l_{-\hat{B}\hat{b}}l_{\hat{B}\hat{x}_{\perp}}+d_{25}l_{-\hat{B}\hat{b}}l_{\hat{B}\hat{x}_{\perp}}+d_{14}l^{2}_{\hat{B}\hat{x}_{\perp}})$
		$G^{C}_{\mathrm{II},y}=1/2\{[d_{36}l_{\hat{E}\hat{x}_{\perp}}l_{-\hat{B}\hat{c}}l_{-\hat{B}\hat{b}}+d_{25}l_{-\hat{B}\hat{b}}(l_{\hat{E}\hat{x}_{\perp}}l_{-\hat{B}\hat{c}}-l_{\hat{E}\hat{c}}l_{\hat{B}\hat{x}_{\perp}})$ $+d_{14}l_{\hat{B}\hat{x}_{\perp}}(l_{\hat{E}\hat{x}_{\perp}}l_{-\hat{B}\hat{c}}-l_{\hat{B}\hat{x}_{\perp}}l_{\hat{E}\hat{c}})]\}$
$K=$III	$j=x$	$G^{A}_{\mathrm{III},x}=0$
		$G^{B}_{\mathrm{III},x}=l_{-\hat{C}\hat{x}_{\perp}}(d_{36}l_{\hat{F}\hat{c}}l_{\hat{C}\hat{b}}-d_{25}l_{\hat{F}\hat{b}}l_{-\hat{C}\hat{c}})$
		$G^{C}_{\mathrm{III},x}=1/2\{l_{\hat{F}\hat{c}}l_{-\hat{C}\hat{x}_{\perp}}l_{\hat{F}\hat{b}}(d_{25}+d_{36})\}$
	$j=y$	$G^{A}_{\mathrm{III},y}=0$
		$G^{B}_{\mathrm{III},y}=-l_{-\hat{C}\hat{x}_{\perp}}(d_{14}l_{-\hat{C}\hat{x}_{\perp}}l_{-\hat{C}\hat{c}}+d_{25}l_{\hat{C}\hat{b}}l_{-\hat{C}\hat{c}}+d_{36}l_{-\hat{C}\hat{c}}l_{\hat{C}\hat{b}})$
		$G^{C}_{\mathrm{III},y}=1/2\{l_{-\hat{C}\hat{x}_{\perp}}(-d_{14}l_{-\hat{C}\hat{x}_{\perp}}l_{\hat{F}\hat{c}}-d_{25}l_{\hat{C}\hat{b}}l_{\hat{F}\hat{c}}+d_{36}l_{-\hat{C}\hat{c}}l_{\hat{F}\hat{b}})\}$

metric angles. The constants G in Table I are linear functions of nonlinear-coefficients d_{36}, d_{25}, d_{14}, and cosines of various geometric angles. These dependencies are explicitly shown in Tables II and III. None of the nonlinear coefficients, and hence F and G, are known. However, as shown below, the explicit expressions for F and G are unimportant for the qualitative conclusions drawn here, except to note that they are material constants and do not change with external fields. The external fields only change the area fractions f_k, and hence the fitting parameters A_j, B_j, and C_j in Table I. The following general conclusions can be drawn.

We begin by observing that in Fig. 4, for an applied electric field along the $+y$ direction, as in our experiments, the electric field would be expected to increase the fraction f_k, $(k=2,4,6,8,10,12)$ of variants with ferroelectric domain polarization components pointing *parallel* to the field, and decrease the fraction f_k, $(k=1,3,5,7,9,11)$ of those variants with polarization components opposite to the field. The reverse would be true for a field along the $-y$ direction. Therefore electric fields $\pm y$ would systematically increase or decrease terms of the sort $f_{1+3-2-4}$, $f_{5+7-6-8}$ and $f_{9+11-10-12}$. The changes to the remaining domain fraction sums under electric fields (e.g., $f_{1+4-2-3}$, and $f_{5+8-6-7}$, etc., in Table I), which we label here as "mixed terms" would, on the average be expected to be negligible. The terms $f_{1+2+3+4}$, $f_{5+6+7+8}$ and $f_{9+10+11+12}$ are *precisely* constants with no expected changes under fields, since these sums are conserved, and the electric fields cannot transform the structural domains I, II, and III into each other.

This discussion in conjunction with Table I, would suggest that for electric-field-induced microstructural bias, the terms A_y^2 and B_y^2 would dominate I_y, and terms C_x^2 would dominate I_x. This is indeed seen in Fig. 5 where $\sin^2(2\theta)$ (associated with C_x^2) dominates the intensity patterns I_x. Similarly, $\sin^2\theta$ and $\cos^2\theta$ terms (associated with A_y^2 and B_y^2) dominate the SHG signal I_y in Fig. 5.

Let us now focus on the changes in the SHG signal $I_y(0°)$ and $I_y(90°)$ due to electric fields [from Figs. 5(a) and 5(c)]. From Eq. (3), for fundamental polarizations at $\theta=0°$ or 90°, the terms that contribute to the SHG signal I_y are A_y^2 or B_y^2, respectively. The changes in $I_y(0°)$ and $I_y(90°)$ observed here, therefore, corresponds to a *net change* in the area fraction of the domain set (1,3,5,7,9,11) with respect to the domain set (2,4,6,8,10,12) in Fig. 3, which is precisely what an electric field along the $\pm y$ axis is expected to do.

Similarly, the change in the experimental intensity I_x with applied field [in Figs. 5(b) and 5(d)] is seen to increase the contribution of the $\sin 2\theta$ term, which in turn indicates an increased contribution from the C_x term. This again is precisely what is expected when there is a net change in domain set (1,3,5,7,9,11) with respect to the domain set (2,4,6,8,10,12) in Fig. 1, with an electric field along the $\pm y$ axis. Hence we conclude that these permanent changes in the SHG signal with external electric fields are consistent with the possible presence of ferroelectric domains in $\mathrm{BiMnO_3}$ films at 82 K.

We note two more important aspects at 82 K. First, the absolute changes in the SHG signal with the application of

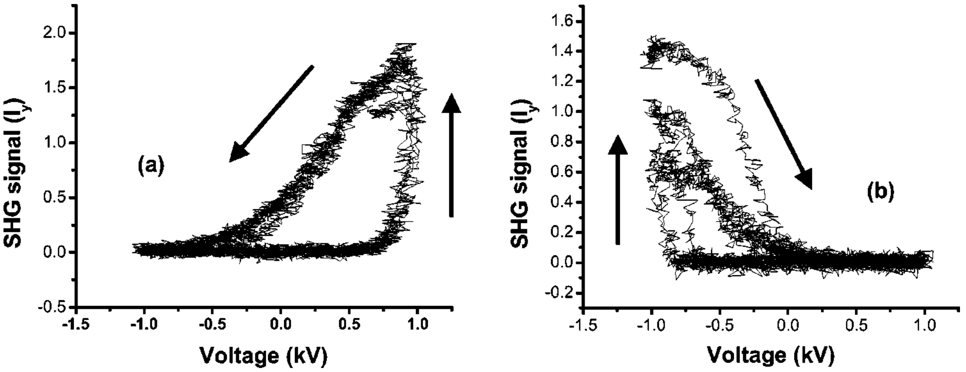

FIG. 6. Hysteresis loops of the SHG intensity $I_y(90°)$ as a function of applied voltage (parallel to the $\pm y$ axis) at 23 °C (a) after applying a steady voltage of $+1$ kV for 30 min and (b) following experiments in (a), applying a voltage of -2 kV for 30 min and then performing voltage cycling experiments shown. Arrows indicate the direction of voltage cycling.

±2 kV appear to be of the order of 1. Second, when the assumption of $\Gamma_{m,j}=0$ in Eq. (3) is lifted, the minima in the polar plots of Figs. 5(c) and 5(d) can be accurately fit. This suggests that a phase change due to optical index differences between different variant classes is finite.

We now turn to field effects at room temperature (296 K). Polar plots similar to Figs. 5(a) and 5(b) are obtained at room temperature as well. Figure 6(a) shows an example of a hysteresis loop of the SHG intensity $I_y(90°)$ as a function of the applied voltage (parallel to the $\pm y$ axis) at room temperature, which corresponds to a net change in area fractions between the odd-numbered and the even-numbered domain sets in Fig. 4, as discussed above. (Actual SHG signals shown in Fig. 6 are nonzero at all fields). Highly asymmetric hysteresis loops are observed, with giant enhancements in one direction as compared to the other direction, indicating a strong internal microstructural bias in the film consistent with poled ferroelectric domain microstructures. This bias can be reversed by the application of a steady electric field in the opposite direction, as shown in Fig. 6(b). Figure 7 shows the time evolution of the SHG signal after a step voltage of -2 kV was applied to the sample, parallel to the $\pm y$ axis. In order to quantify the SHG enhancement, we compare the maximum signal with that for a *z*-cut $LiTaO_3$ reference, using the $d_{22}=1.672$ pm/V coefficient in the following equation:

$$d_f^2=d_r^2\left(\frac{P_f^{2\omega}}{P_r^{2\omega}}\right)\left(\frac{P_r^{\omega}}{P_f^{\omega}}\frac{T_r^{\omega}}{T_f^{\omega}}\right)^2\frac{A_f}{A_r}\left(\frac{n_f^{\omega}}{n_r^{\omega}}\right)^2\frac{n_f^{2\omega}}{n_r^{2\omega}}\left(\frac{l_{c,r}}{l_{c,f}}\right)^2\frac{e^{-\alpha_r^{2\omega}l_{c,r}}}{e^{-\alpha_f^{2\omega}l_{c,f}}}, \tag{4}$$

where the subscripts r and f refer to the reference and the film, respectively, $P^{2\omega}(P^{\omega})$ are the second harmonic (fundamental) signal powers measured, T is the transmission coefficient of the fundamental, A is the area of the probed beam diameters, n are the indices of refraction, l_c the coherence lengths, and α the absorption coefficient of the film at 2ω. Using spectroscopic ellipsometry, the refractive indices of the film were determined as $n_f^{2\omega}=1.88+0.8j$ and $n_f^{\omega}=2.217+0.56j$.[14] The beam areas were $A_f=\pi(63\ \mu\text{m})^2$ and $A_r=\pi(57\ \mu\text{m})^2$ and the powers were $P_f^{\omega}=580$ mW, $P_r^{\omega}=27$ mW. Since the calculated coherence length $l_c \sim 1.33\ \mu$m for $BiMnO_3$ is much larger than the film thickness ($l_f \sim 110\pm 29$ nm), we assume $l_{c,f}=l_f=110$ nm in the above relation. Even without accounting for film absorption at 2ω through the last ratio in Eq. (4), the effective $d_f \exp[(\alpha_r^{2\omega}l_{c,r}-\alpha_f^{2\omega}l_f)/2] \sim 16.5$ pm/V. Taking the absorption into account, the estimated $d_f \sim 193$ pm/V. As a comparison, the d_{33} for well-known nonlinear material $LiNbO_3$ is ~36 pm/V.[15] Such giant dc field (E^0) induced second harmonic response can arise from ferroelectric domain alignment, as well as third order nonlinear optical process, where nonlinear polarization $P_i^{2\omega} \propto \chi_{ijkl}(\omega,\omega,0)E^{\omega}E^{\omega}E^0$ is created in the film, and the superscripts indicate the frequencies.

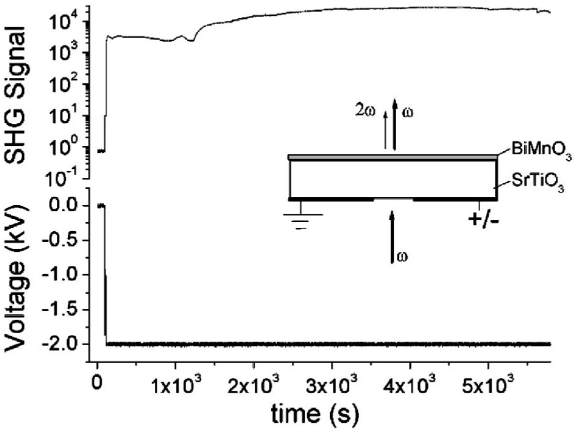

FIG. 7. Time evolution of the SHG signal after a -2 kV voltage step is applied at 23 °C. The inset shows the geometry of SHG measurement and of voltage application across a 2 mm electrode gap. The peak enhancement of the SHG signal is around 35 000 times.

A related third-order optical nonlinearity is $\chi_{ijkl}(\omega,-\omega,\omega)$, giving rise to intensity (I) dependent index change $\Delta n=n_I I$ and absorption change $\Delta\alpha=\alpha_I I$. These coefficients were measured using the single beam *z*-scan technique[16] at 900 nm with 140 fs pulses with peak intensity at focus of 1.3 GW/cm^2.[14] Both closed and open aperture scans were performed on $BiMnO_3$ films to extract the nonlinear optical coefficients. At room temperature (296 K) the nonlinear absorption coefficient was measured to be $\alpha_I \sim -0.08$ cm/kW and nonlinear refractive index as $n_I \sim -0.53 \times 10^{-9}$ cm^2/W. These values did not change with the frequency of the chopping of the incident beam from 97 Hz to 3.24 kHz, suggesting that the origin is not thermal in nature. These are large values as compared to films such as Rh:$BaTiO_3$ deposited on $SrTiO_3$ (Ref. 13) and $SrBi_2Ta_2O_9$ on quartz,[17,19] but smaller than Bi films on glass.[18]

There are many plausible explanations for the observed nonlinear optical behavior. Domains of different variants probed by the beam contribute to SHG signal.[13] Under the influence of external electric fields, the ferroelectric domains realign and the radiated SHG signals from these domains interfere constructively to enhance the SHG signal.[12] This is one explanation for the pronounced dependence of SHG signal on the applied electric field. Another mechanism for the SHG enhancement with applied fields may be a result of competition between charge transfer and electron correlation similar to that discussed in Refs. 20–23. The large nonlinear response observed at room temperature and above is accompanied by dielectric losses in the films. There could be a correlation between the two, with some contribution from free-carrier absorption. In such a case, a plausible charge transfer mechanism may be between a $6p$ orbital of Bi and a $3d$ orbital of Mn via a $2p$ orbital of O_2.[21–23] A third possibility is that the material may be an *electronic* ferroelectric,[24] where polarization arises from a condensation of an exciton electron-hole pair (plausibly an itinerant Bi-$6p$ electron and a localized Mn-$3d$ hole). This third possibility has been predicted to result in giant second harmonic enhancement at specific resonance frequencies.[24]

To conclude, we observe electric-field-induced permanent changes in the second harmonic response from a $BiMnO_3$ thin film. These changes are shown to be consistent with the possible presence of ferroelectricity in $BiMnO_3$ films using external electric fields. Three-to-four orders of magnitude enhancement in optical second harmonic response from a 900 nm incident light was observed at room temperature under external fields of $\sim$707 V/mm. Large nonlinear refraction (n_I) and absorption coefficients (α_I) were measured as well. Further investigations are presently underway in understanding the origin of these nonlinear optical effects.

We would like to acknowledge valuable discussions with Dr. Nicola Spaldin, and the help of Dr. Isli An and Chi Chen with ellipsometry. This work was supported by a grant from the National Science Foundation through Grant Nos. DMR-9984691 and DMR-0103354.

---

*Deceased.

[1] H. Schmid, Ferroelectrics **162**, 317 (1994).

[2] M. Fiebig, Th. Lottermoser, D. Fröhlich, A. V. Goltsev, and R. V. Pisarev, Nature (London) **419**, 818 (2002).

[3] N. A. Hill and K. M. Rabe, Phys. Rev. B **59**, 8759 (1999).

[4] A. Moreira dos Santos, S. Parashar, A. R. Raju, Y. S. Zhao, A. K. Cheetham, and C. N. R. Rao, Solid State Commun. **122**, 49 (2002).

[5] E. Ohshima, Y. Saya, M. Nantoh, and M. Kawai, Solid State Commun. **116**, 73 (2000).

[6] H. Faqir, H. Chiba, M. Kikuchi, Y. Syono, M. Mansori, P. Satre, and A. Sebaoun, J. Solid State Chem. **142**, 113 (1999).

[7] H. Chiba, T. Atou, and Y. Syono, J. Solid State Chem. **132**, 139 (1997).

[8] T. Kimura, S. Kawamoto, I. Yamada, M. Azuma, M. Takano, and Y. Tokura, Phys. Rev. B **67**, 180401(R) (2003).

[9] T. Atou, H. Chiba, K. Ohayama, Y. Yamaguchi, and Y. Syono, J. Solid State Chem. **145**, 639 (1999).

[10] A. F. Moreira dos Santos, A. K. Cheetham, W. Tian, X. Pan, Y. Jia, N. J. Murphy, J. Lettieri, and D. G. Schlom, Appl. Phys. Lett. **84**, 91 (2004).

[11] V. Gopalan and R. Raj, J. Am. Ceram. Soc. **79**, 3289 (1996); J. Appl. Phys. **81**, 865 (1996); Appl. Phys. Lett. **68**, 1323 (1996).

[12] Y. Barad, J. Lettieri, C. D. Theis, D. G. Schlom, V. Gopalan, J. C. Jiang, and X. Q. Pan, J. Appl. Phys. **89**, 1387 (2001); **89**, 5230 (2001); **90**, 3497 (2001).

[13] M. Fiebig, D. Fröhlich, Th. Lottermoser, and M. Maat, Phys. Rev. B **66**, 144102 (2002).

[14] A. Sharan, I. Ahn, C. Chen, R.W. Collins, J. Lettieri, D. Schlom, and V. Gopalan, Appl. Phys. Lett. **83**, 5169 (2003).

[15] W. Yue and J. Yi-jian, Opt. Mater. (Amsterdam, Neth.) **23**, 403 (2003).

[16] M. Sheik-Bahae, A. A. Said, T. H. Wei, D. J. Hagan, and E. W. Stryland, IEEE J. Quantum Electron. **26**, 760 (1990).

[17] G. Yang, H. G. Tan, A. Jiang, Y. Zhou, and Z. Chen, Appl. Opt. **41**, 1729 (2002).

[18] Y. Z. Gu, W. F. Zhang, D. H. Gu, and F. Y. Gu, Opt. Lett. **26**, 1788 (2001).

[19] W. F. Zhang, M. S. Zhang, Z. Yin, Y. J. Gu, Z. L. Du, and B. L. Yu, Appl. Phys. Lett. **75**, 902 (1999).

[20] D. R. Liu, K. S. Wu, M. F. Shih, and M. Y. Chern, Opt. Lett. **27**, 1549 (2002).

[21] H. Kishida, H. Matsuzaki, H. Okamoto, T. Manabe, M. Yamashita, Y. Taguchi, and Y. Tokura, Nature (London) **405**, 929 (2000).

[22] G. P. Zhang, Phys. Rev. Lett. **86**, 2086 (2001).

[23] R. T. Clay and S. Mazumdar, Phys. Rev. Lett. **89**, 039701 (2002).

[24] T. Porentgen, Th. Östreich, and L. J. Sham, Phys. Rev. B **54**, 17 452 (1996).